CSIRO PUBLISHING

International Journal of Wildland Fire **2009**, *18*, 302–309 www.publish.csiro.au/journals/ijwf

Generation of synthetic infrared remote-sensing scenes of wildland fire

Zhen Wang[A], *Anthony Vodacek*[A,C] *and Janice Coen*[B]

[A]Center for Imaging Science, Rochester Institute of Technology, 54 Lomb Memorial Drive, Rochester, NY 14623, USA.

[B]National Center for Atmospheric Research, PO Box 3000, Boulder, CO 80307, USA.

[C]Corresponding author. Email: vodacek@cis.rit.edu

Abstract. We describe a method for generating synthetic infrared remote-sensing scenes of wildland fire. These synthetic scenes are an important step in data assimilation, which is defined as the process of incorporating new data into an executing model. In our case, this is a fire propagation model. The scenes are built using the surface output of fire position from a fire propagation code and prior knowledge of fire physics and behavior to estimate the shape of the flame. The scene radiance is then estimated by employing a physics-based ray-tracing model called DIRSIG to render the radiation that would reach a sensor on an airborne platform. Values of the Fire Radiated Energy calculated from the synthetic radiance scene compare well with previously published values, providing validation of the method.

Additional keywords: DIRSIG, fire propagation models, fire radiative energy, flame height, heat flux.

Introduction

Two geospatial technology tools that find increasing use in wildland fire management are high-resolution remote sensing and fire propagation models. Wildland fire researchers are continually improving these tools for monitoring and predicting wildland fire movement, respectively.

High-resolution image collection, whether from satellite or airborne sensors, can be very effective in quickly providing synoptic fire position information (see Lentile *et al*. 2006 for a review). For example, the United States Department of Agriculture Forest Service operates an airborne infrared line scanner called Phoenix that is operationally deployed at major wildland fire events (Greenfield *et al*. 2003). Other demonstrations of effective use of remote-sensing technologies for mapping fire locations rely on advanced processing techniques for delivering products in near real time (Radke *et al*. 2000; Ambrosia *et al*. 2003; Riggan *et al*. 2004; McKeown *et al*. 2005). These fire detection systems typically detect Planck-type radiation in the shortwave, midwave, and longwave portions of the infrared spectrum (1–3, 3–5, and 8–20 μm), although emission and absorption lines can also be used for detecting fires (Vodacek *et al*. 2002; Dennison 2006).

Whereas remote fire detection systems focus on monitoring and real-time detection, fire propagation models are designed to provide a forecast of future fire behavior. A variety of approaches to fire propagation modeling have been developed, ranging from semi-empirical models to computational fluid dynamics approaches. Rothermel (1972) formulated a semi-empirical model using a physics-based approach with calibration based on observations under different weather, terrain, and fuel conditions. FARSITE is an example of a fire behavior model based on the basic propagation equations of Rothermel (Finney 1998). Another approach has been based on fire physics described with differential equations (e.g. Weber 1991; Asensio and Ferragut 2002). The National Center for Atmospheric Research (NCAR) coupled atmosphere–fire model tracks smoke and hot gases in the atmosphere and is able to represent the complex interactions between the fire and local winds, although the basic propagation uses Rothermel's equations (Clark *et al*. 1996, 2004; Coen 2005). The Fire Dynamics Simulator (FDS) is a full computational fluid dynamics code that solves numerically a form of the Navier–Stokes equations appropriate for low-speed, thermally driven flow with an emphasis on smoke and heat transport from fires (Mell *et al*. 2007). Another well-used computational fluid dynamics code is FIRETEC (Linn 1997). Many of these models are undergoing continual revision and improvement. Weber (1991), Pastor *et al*. (2003), and Mell *et al*. (2007) provide in-depth reviews of these and other fire propagation models.

The use of remote sensing and separate fire propagation simulations helps provide the answers to questions about current and future fire behavior. However, little work has been directed at bringing these two technological tools together in a single system. The concept of an integrated observation and simulation system, where the remote-sensing observations are used to steer the simulation results falls within the realm of data assimilation. Data assimilation is defined to represent the process where simulations respond to new data that arrives while the computer model is running. The idea of data assimilation can be extended by adding a feedback capability to the modeling system, where the simulation will steer new data collection efforts with the goal of improving forecasts by reducing uncertainty (Darema 2004). These systems are intended to be computationally fast and to some extent can trade off physical correctness of the modeling process for simplification and speed and rely on data

 10.1071/WF08089 1049-8001/09/030302

assimilation to maintain accuracy. Thus, a critical aspect of a simulation system is the ability to assimilate data from a variety of measurement systems. The most extensive examples of environmental data assimilation where observations are compared with environmental models come from ocean circulation and weather forecasting efforts (e.g. Derber and Rosati 1989; Anderson 1996; Malanotte-Rizzoli and Tziperman 1996; Barker *et al*. 2004).

We are currently working on the application of data assimilation techniques to the wildland fire propagation problem and the details of our overall approach, which is based on the NCAR coupled model described above, can be found elsewhere (Douglas *et al*. 2006; Mandel *et al*. 2008). The present paper describes an initial approach to generating synthetic infrared remote-sensing scenes of a wildland fire using the NCAR model outputs. In the working simulation, this prediction of infrared scene radiance is made for the state of the model at the time corresponding to the time that airborne remote-sensing images are obtained. The synthetic scene is then compared with the real observations of infrared radiance in the data assimilation step and the model is adjusted to better match the real observations.

The synthetic scene output depends on the NCAR model output variables such as the heat flux and the wind speed. The use of the variables from the model allows us to estimate the flame shape used in simulating radiance from the fire scene. Given the flame shape, we assume we can adequately estimate the infrared scene radiance by including three aspects of radiated energy. These are: (1) radiation from the hot ground under the fire front and the cooling of the ground after the fire front passes. This accounts for the heating and cooling of the surface. (2) The direct radiation to the sensor from the three-dimensional flame. This accounts for the intense radiation from the flame itself. (3) The radiation from the three-dimensional flame that is reflected from the nearby ground. This reflected radiation is most important in the near and midwave infrared spectrum. Reflected longwave radiation is much less important because of the high emissivity (low reflectivity) of burn-scar in the longwave infrared portion of the spectrum (Kremens *et al*. 2003). We are not including the preheating of the ground and vegetation in front of the advancing fire, only determining the reflection of fire radiation from the vegetated ground surface. At this early stage of synthetic image development, we are assuming the preheating of the vegetation and ground in front of the advancing fire is a secondary effect within the overall remote-sensing scene phenomenology that could be added later if desired. To our knowledge, this is the first attempt to synthesize the radiance of an entire high-resolution infrared remote-sensing scene of a wildland fire.

Methods

The synthetic scene generation method developed here uses the output of a simulated grassfire using the NCAR model. The simulation domain is 4200 by 4200 m on flat terrain with a wind speed of 3 m s^{-1} and tall grass as the fuel type, and a line ignition. We now describe the methods for including the fire direct radiation, reflected radiation, and burn-scar cooling in the scene generation model. Then we describe the synthetic image generation model procedures that are used for rendering the synthetic remote-sensing scene using the Wildfire Airborne Sensor Program (WASP) sensor configuration with ray tracing done by the Digital Imaging and Remote-sensing Image Generation model (DIRSIG).

Surface radiation and burn-scar cooling

We begin with a simulation of the ground surface temperature of the fire scene. For our simulations, we assume 1073 K is the highest ground temperature under the fire front based on typical temperatures in wildland fires (Kremens *et al*. 2003). Preheating ahead of the fire front is a complex process relating to the fuel type, fuel density, humidity, and other processes and we do not account for the simulation of this complex process, so there is a simple jump from ambient ground temperature to 1073 K at the leading edge of the fire front.

After the flame front passes, the ground immediately begins cooling. To a first order, we could assume Newton's law of cooling (a simple exponential cooling behavior), but some of the few field measurements of ground cooling after the passage of a fire front suggest that for some cases, a double exponential is a better model of burn-scar cooling, with a slow component that may be due to heat slowly released by soil water. Based on the measurements of Kremens *et al*. (2003), we fit a double exponential to their temperature data obtained from thermocouples placed at the soil surface by using the following equation:

$$T_t = T_1 e^{-t/\tau_1} + T_2 e^{-t/\tau_2} + T_a \quad (1)$$

where t is the time since ignition; T_t is the temperature of the burn-scar at time t; T_1 (579°C) and τ_1 (75 s) are the peak temperature and fast time constant; T_2 (197°C) and τ_2 (247 s) are the peak temperature and slow time constant; and T_a is the ambient ground temperature, which is constant at 34°C. The sum of T_1, T_2 and T_a was constrained to 1073 K and the amoeba iterative optimization procedure was used find the best fit parameters listed here (Press *et al*. 2007). This single set of parameters was used to estimate the temperature for all cooling surface pixels.

To identify the fire position during the simulation, we used the surface fire sensible heat flux output of the NCAR model. Using trial and error, a threshold value for the heat flux is set and the pixels with heat flux above the threshold are labeled as the fire front and assigned a temperature of 1073 K. As the simulation progresses in time, those pixels eventually fall below the threshold and begin cooling. By keeping track of the time since the fire front has passed, the surface temperature can be calculated with Eqn 1. Unburned areas are the pixels where there is zero heat flux and those pixels are assigned the ambient temperature of 34°C. Fig. 1 shows the temperature map at two times during the simulation. The brightest area is the fire front and shades of gray correspond to surface cooling behind the fire front. This surface temperature map is later used to generate the surface radiance.

Flame height estimation

After predicting the ground temperature, the next step is to create a flame shape for the flame front by again using the sensible heat flux output of the NCAR model. Larger heat flux is translated into tall flames and smaller heat flux is translated into short flames. The flame shape is built by defining grid points that are the corners of cubic 'voxels'. Deflection of the flame by the local wind is added and each voxel is randomly shifted to generate a more varied structure. This procedure is meant to capture the

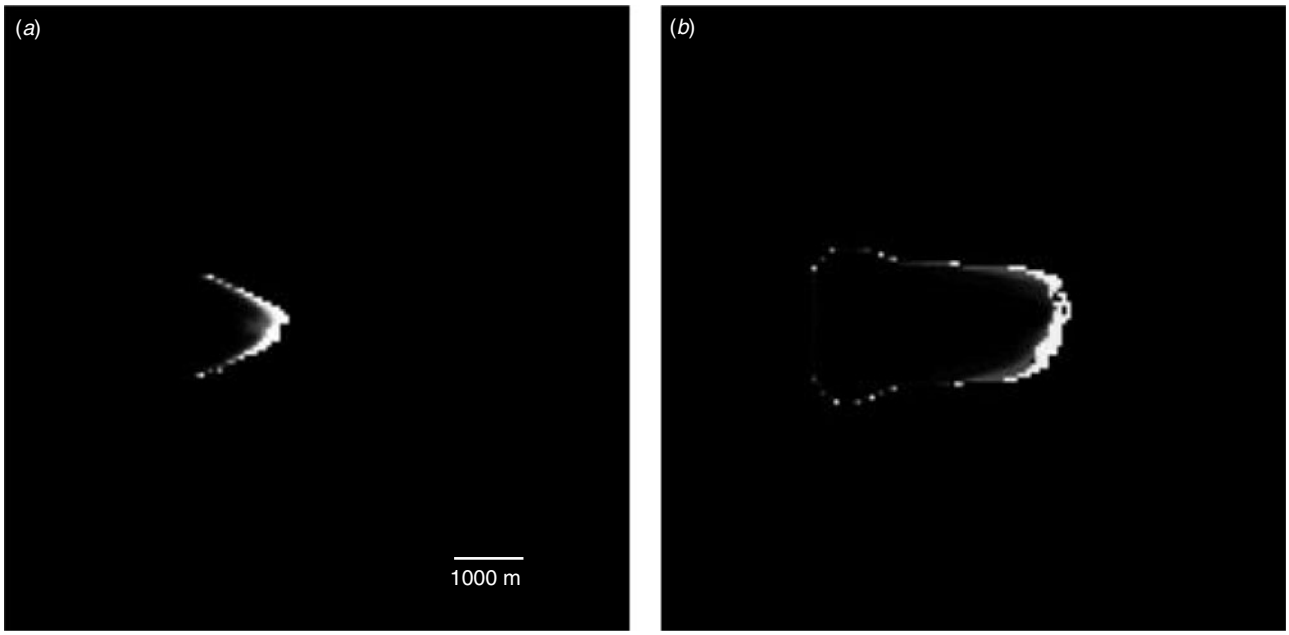

Fig. 1. Temperature maps showing the fire location as white and cooling ground behind the fire as shades of gray; (*a*) 16 min after ignition; and (*b*) 74 min after ignition.

essence of the flame structure and is not an exact representation of the flame at that time step of the model. Overall our goal is to estimate reasonable values of the flame radiance, rather than the complex turbulence and complicated spatial configuration of a real flame, which is often the goal of high-resolution simulations by the graphics community.

Experimental studies showed that the flame volume is directly proportional to the heat-release rate of the fire:

$$V_f = Q/Q' \tag{2}$$

where V_f is the flame volume; Q is the total heat release rate of the fire; Q' is the heat release rate per unit flame volume, an estimated constant value of 2000 kW m^{-3} (McGratten *et al.* 2007). We also assume proportionality between the heat release rate and the heat flux Q_h:

$$Q \propto Q_h \tag{3}$$

Further, the flame volume V_f is proportional to the product of fire ground area and flame height l_f. If the fire front has length w_1 along the direction of fire propagation and width w_2 perpendicular to the direction of fire propagation:

$$V_f = l_f w_1 w_2 \tag{4}$$

Substituting Eqns 3 and 4 into Eqn 2 and rearranging, the flame height l_f can be estimated by:

$$l_f = \frac{Q_h}{Q' w_1 w_2}\alpha \tag{5}$$

where α is a scale coefficient and the heat flux and ground dimensions are from the propagation model output. The adjustable scale coefficient α is added according to fuel type to make the predicted flame size reasonable. In the simulation performed here for a grassland fire, α was chosen to provide an average flame height of ~2 m, but the flame heights will be higher or lower depending on the value of the heat flux. We also constrain the estimated flame height of each time step within one standard deviation from the heights of all the previous time steps; thus the flame height of each time step will not deviate greatly from the previous or following time step when there is no dramatic change of environmental conditions.

Flame-tilt in wind

Besides terrain, fuel type and amount, wind plays an important role in energy transfer direction and rate as flame is deflected by air movement. The extent of flame-tilt will depend on the wind velocity. According to Drysdale (1998) and references therein, the effect of wind speed V' on fires is:

$$\sin\theta = 1 \text{ for } V' < 1 \tag{6}$$

$$\sin\theta = (V')^{-1/2} \text{ for } V' > 1 \tag{7}$$

where θ is the tilt angle from the vertical to the front of the flame, as shown in Fig. 2. V' is estimated from V, the dimensionless windspeed defined below:

$$V' = V\left(\frac{2c_p T_\infty \rho_\infty}{\pi \rho_f \Delta H_c}\right)^{1/3} \tag{8}$$

In Eqn 8, c_p is air thermal capacity at constant pressure, 1040 J kg^{-1} K^{-1}; T_∞ is the ambient air temperature, 300 K; ρ_∞ is ambient air density, 1.18 kg m^{-3}; ρ_f is fuel vapor density, 0.36 kg m^{-3}, an estimate that is a little larger than air density

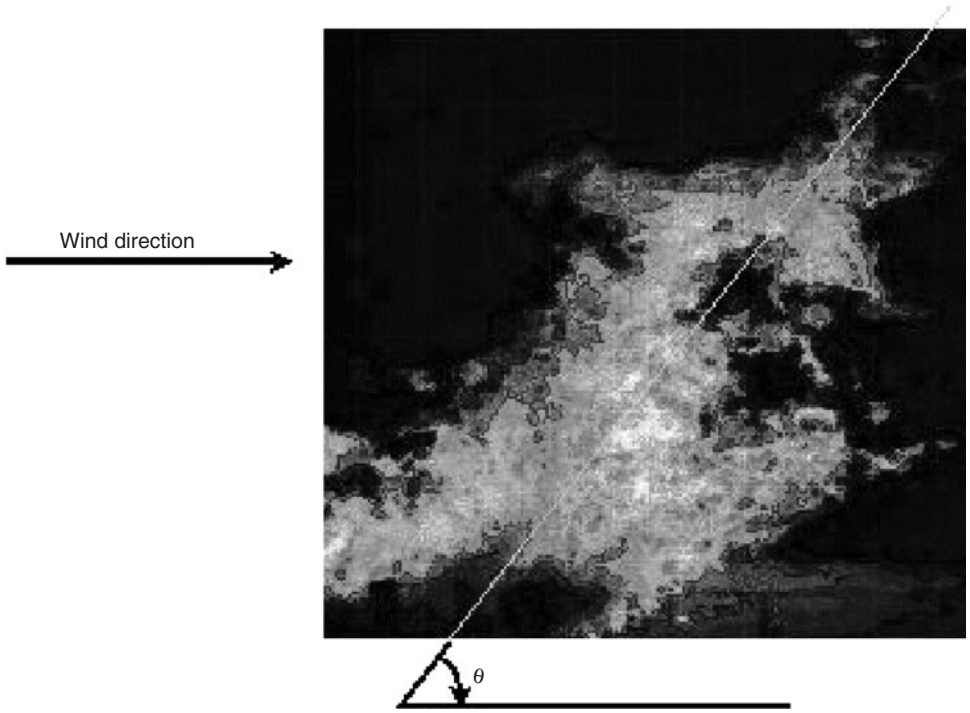

Fig. 2. Deflection of a flame by wind.

($0.32\,\mathrm{kg\,m^{-3}}$) at a temperature of 1100 K; and ΔH_c is heat of combustion, a value of $16\,515\,\mathrm{kJ\,kg^{-1}}$ taken from Brown and Davis (1973). V is the only variable in this equation and is a dimensionless wind speed given by v/u where v is the actual wind speed, and u is a characteristic vertical fire plume velocity, in $\mathrm{m\,s^{-1}}$, given by:

$$u_{\max} = 1.9Q^{1/5} \tag{9}$$

where Q is the rate of heat release (Drysdale 1998). We again use heat flux in place of the heat release rate by assuming proportionality. Although the units are incorrect and the value is only proportional, the small value of the exponent means that the plume velocity is only very weakly dependent on the heat release rate and this result produces reasonable results as shown in Fig. 3. The 3-$\mathrm{m\,s^{-1}}$ wind speed produces a flame-tilt of ~45° or slightly more, which is in accordance with the rule of thumb that a 2-$\mathrm{m\,s^{-1}}$ wind speed produces flame-tilt of ~45° (Drysdale 1998). The flames will have slightly different deflection angles according to the magnitude of the heat flux. After flame is deflected, small random deviation from a uniform distribution are added to xy coordinates of the voxel positions to give the fire a more turbulent appearance.

The overall method to generate the flame shape utilizes the heat flux and wind field to provide real-time prediction of flame height and tilt angle. By iteratively solving Eqns 5–8 while updating the constraint of flame scale, unique solutions to flame height and deflection angle will be obtained for each ground pixel with high heat flux at each time step, and the flame geometry will be uniquely defined.

Volume rendering in DIRSIG with the voxelized space

Based on the heat flux and local winds from the simulation and the methods described above, we are able to simulate the temperature for the surface as an array of pixels and the flame shape as an arrangement of voxels.

In this section, we describe the ray tracing method for determining the radiance from those sources as they would be viewed by an airborne remote-sensing system. The ray tracing code used is the DIRSIG model. The DIRSIG model is a synthetic image-generation model based on first principles. The model is developed and maintained by the Digital Imaging and Remote Sensing Laboratory at the Rochester Institute of Technology (Schott *et al*. 1999; Digital Imaging and Remote Sensing Laboratory 2006). The model can produce multi- or hyperspectral imagery from the visible through the thermal infrared region of the electromagnetic spectrum. Note that the terms and equations describing radiation properties in this section are all a function of wavelength, although we leave off the wavelength notation for simplicity.

The concept of determining radiance from the flame shape is similar to other work on modeling the radiation component of fire propagation. For example see Knight and Sullivan (2004; Fig. 1), where the flame is modeled as a triangular prism to determine radiation to the surrounding ground and fuel. In our case, we consider the radiation from the three-dimensional flame and also consider radiation from the ground toward the sensor and radiation reflected from the ground near the flame toward the sensor. The scene radiance is an accumulation of brightness that is a function of the temperature, distance from the sensor, material type, and atmospheric transmission from ground level to

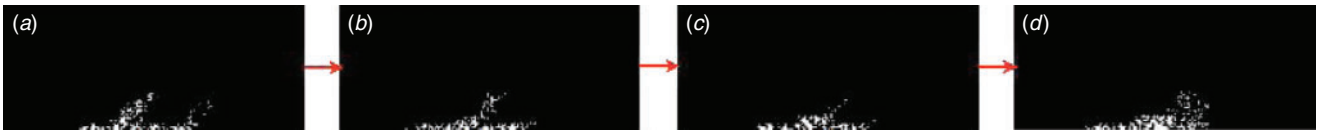

Fig. 3. Side projection of estimated flame evolution with flame voxels shown in white; (*a*) 61 min 18 s after ignition; (*b*) 12 s later than (*a*); (*c*) 24 s later than (*a*); (*d*) 36 s later than (*a*). Each voxel is represented by a white dot in this visualization; the actual voxel sizes used in the ray tracing are larger.

the sensor. DIRSIG uses the MODTRAN atmospheric radiative transfer code for calculating the optical properties of the atmosphere (Anderson *et al*. 2000). A sensor module allows the input of sensor characteristics that modify the scene as if it was viewed through an imaging sensor. With the volume-rendering method, when a ray, cast from the sensor toward the scene, encounters a region containing fire that was precomputed by the external fire model, the simulation determines how many integration steps to process through the fire, or how many voxels containing fire are on the path of the ray, and path length within each of the voxels. The physical properties of each voxel are variables such as temperature, optical depth, and distance from the sensor.

Fig. 4 shows how a ray passes through a grid to the sensor, where τ_i is the transmission of each grid square on the ray path. The additive projection is a summation of emitted and transmitted radiance from all the voxels on the ray path. The transmission properties of participating voxels are characterized by the path length for the ray and the fire attenuation coefficient. The attenuation coefficient was set to a low value of $\sim 0.05\,\mathrm{m}^{-1}$ across the shortwave and midwave infrared. If there are n flame voxels between the bottom of the flame and the sensor, then the contribution to the received radiance due to the self-emitted radiance from the ith voxel can be expressed as:

$$\Delta L_i = L_i(\tau_i - \tau_{i+1}) \tag{10}$$

where the indexing scheme for the fire voxels is defined to begin at the sensor and end with the voxel at the bottom of the flame. L_i is the radiance due to the temperature of the ith voxel, τ_i is the transmission along the sensor-target path from the sensor to the top of the ith voxel, and is the product of transmission of all j voxels between the ith voxel and the sensor:

$$\tau_i = \prod_{j=1}^{i=1} \Delta\tau_j = \prod_{j=1}^{i-1} e^{-\delta_j} \tag{11}$$

where $\Delta\tau_i$ is the transmission of the ith homogeneous flame voxel and δ_j is the optical depth of the voxel j along the path to the sensor. By substituting Eqn 11 in Eqn 10 and summing the radiance from each single voxel, the total contribution to radiance, L, from all n voxels can be obtained:

$$L = \sum_{i=1}^{n} \Delta L_i = \sum_{i=1}^{n} L_i \left(\prod_{j=1}^{i-1} \Delta\tau_j - \prod_{j=1}^{i} \Delta\tau_j \right) \tag{12}$$

Radiance from the ground itself is determined and radiance from the fire that is reflected by the nearby ground is calculated. All of these sources of radiance are then attenuated by the atmosphere along the path to the sensor.

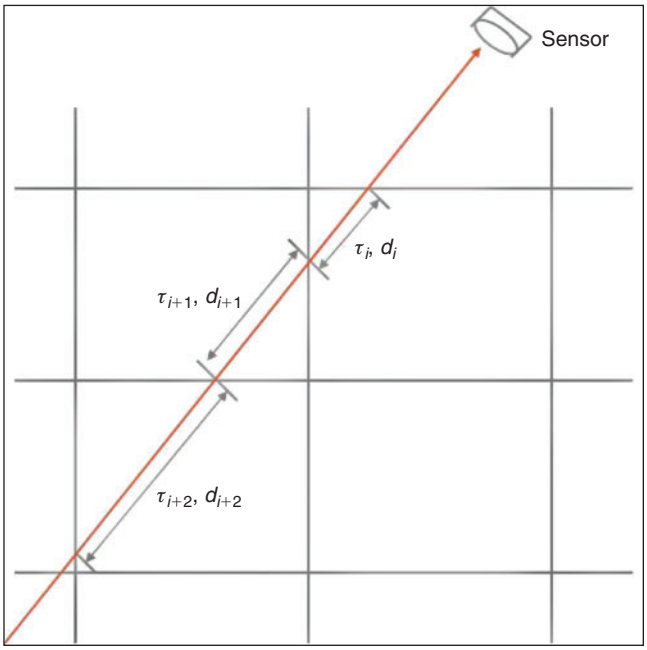

Fig. 4. A ray cast through a regular grid. τ is the transmission and d is the path length through the ith voxel.

Results

The DIRSIG rendering of the infrared radiance from the grassfire at night as it would be observed by the WASP sensor is shown in Fig. 5. The sensor model in DIRSIG was set to the WASP specifications: the cameras have a focal length of 25 mm and there are 640 by 512 pixels each for the shortwave, midwave, and longwave infrared cameras. The cameras are put at the nominal operating altitude of ~3000 m producing a pixel ground spot size of ~3 m. The sensor is looking at a slant angle of ~25° from nadir.

Verification

After estimating the flame geometry and generating the synthetic multispectral remote-sensing wildfire scene, we can provide verification of our results by examining the fire radiative energy (FRE) determined for the synthetic scene relative to previous work (Kaufman *et al*. 1996; Wooster *et al*. 2003).

As a first step toward verification, we calculated the FRE of a hotspot pixel based on temperature and retrieved spatial extent of the thermal components within the area. This is the FRE_{TRUE} parameter of Wooster *et al*. (2003). The active fire pixels in our synthetic remote-sensing scene are not homogeneous and are a mixture of several thermal components each having a different

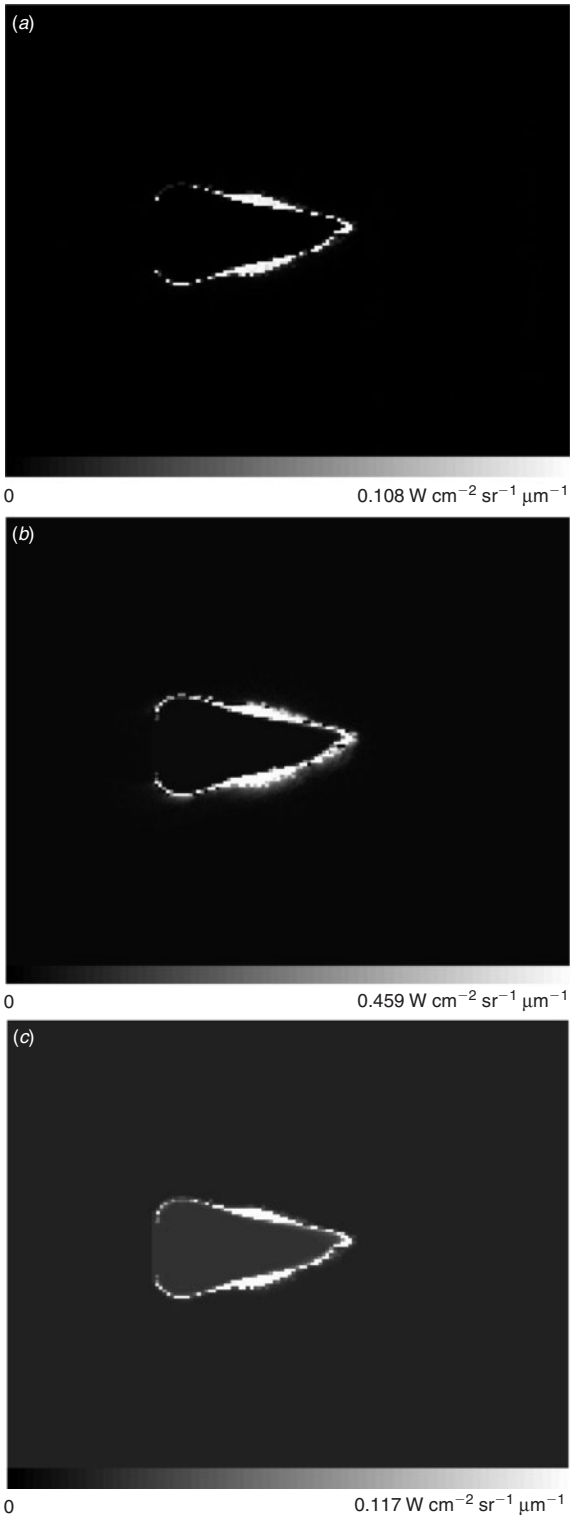

Fig. 5. DIRSIG rendering of the infrared grassfire scene ~1 h after ignition using the Wildfire Airborne Sensor Program (WASP) sensor specifications. (*a*) Shortwave infrared channel (0.9–1.7 μm); (*b*) midwave infrared channel (3–5 μm); (*c*) longwave infrared channel (8–11 μm). The units of these radiance images are watts per square centimetre per steradian per micrometre (W cm^{-2} sr^{-1} μm^{-1}).

temperature and fractional area. In our simulation, each ground pixel in the scene has an area of 3 × 3 m. With this scale, hotspot pixels might be composed of unburned vegetation, flame and the hot ground below the flame, and burn-scar. The total FRE_{TRUE} from all fire thermal components in a pixel can be calculated as:

$$FRE_{TRUE} = A_{sample}\varepsilon\sigma \sum_{i=1}^{n} A_i T_i^4 \quad (13)$$

where FRE_{TRUE} is fire radiative energy, J s^{-1}; A_{sample} is the ground sampling area, m^2; ε is emissivity; σ is the Stefan–Boltzmann constant, 5.67×10^8 J s^{-1} m^{-2} K^{-4}; A_i is the fractional area of the *i*th thermal component within a specific ground pixel, and T_i is the temperature of *i*th thermal component, K (Wooster *et al*. 2003).

The ground temperature under the active fire is set to be 1100 K, which is the highest temperature observed by Kremens *et al*. (2003), the mean flame temperature is set at 1000 K, and the smouldering scar is 600 K (Wooster *et al*. 2003). A stepwise linear unmixing algorithm was performed on each pixel of the synthetic multispectral wildfire scene to calculate the fractional area of each thermal component.

If we leave out the sample area from Eqn 13, the units for FRE_{TRUE} are J s^{-1} m^{-2} (i.e. see Wooster *et al*. 2003; table 2). We determined the total FRE_{TRUE} per unit area by summing the contribution from all thermal components for the subset of pixels that had a flaming fraction. The FRE_{TRUE} per unit area for these pixels ranges from 7.31×10^4 to 7.47×10^4 J s^{-1} m^{-2}. These are total values above the background and potentially include contributions from each of the components based on the unmixing fractions. These values are slightly higher than the FRE_{TRUE} per unit area for the flaming fraction in table 2 of Wooster *et al*. (2003). This is reasonably close agreement with the results of Wooster *et al*. (2003), given that the parameters of our unmixing model were different because we included the separation of the ground temperature and the flame temperature and because the ground temperature (based on field measurements) was higher than the flaming temperature in their work.

A more realistic test of our results is determining the FRE from the midwave infrared radiance (FRE_{MIR}) value based on eqn 5 in Wooster *et al*. (2003) because in our case the value is obtained from the synthetic radiance scene:

$$FRE_{MIR} = \frac{A_{sample}\sigma\varepsilon}{a\varepsilon_{MIR}} L_{MIR,h} \quad (14)$$

where $L_{MIR,h}$ is the midwave infrared radiance of fire pixels, ε_{MIR} is the fire emissivity in the midwave infrared, and a is a constant related to the sensor. As the midwave WASP band is similar to that of the Hot Spot Recognition Sensor (HSRS) on the Bi-spectral InfraRed Detection (BIRD) platform, for a we used the value of 3.3×10^{-9} provided for the HSRS midwave infrared band by Wooster *et al*. (2003). The total FRE_{MIR} per unit area for pixels with a flaming component ranged from 6.02×10^4 to 7.89×10^4 J s^{-1} m^{-2}, bounding the value of 6.36×10^4 J s^{-1} m^{-2} for the flaming component alone in table 2 of Wooster *et al*. (2003). This is good evidence that our synthetic scene is a valid representation of fire infrared radiance.

Discussion

Our method for creating synthetic infrared remote-sensing scenes of wildland fire uses information from a surface fire propagation model and knowledge of fire physical properties to estimate fire spectral radiance. A grassland fire scene is rendered using a physics-based ray tracing model, DIRSIG, that accounts for radiation from the ground surface, radiation from the flame, any reflected radiation from the ground near the fire, and atmospheric transmission. The visualization of the scene can be made for a variety of spectral responses and spatial resolutions of different sensors. Values of FRE calculated from the synthetic scene midwave infrared radiance provide confirmation that the radiance produced by the method is valid. Given the output of a fire propagation model, the generation of the synthetic scene takes less than 3 minutes of computation time on a Sun Blade 1500 workstation (Sun Microsystems, Santa Clara, CA).

The use of a physics-based image-generation model like DIRSIG provides a means for very accurate rendering of the scene, both spectrally and spatially. A general assumption of the approach is that the fire radiation is a black body or gray body. Improved measurements of fire spectral radiation could be used to modify these assumptions and improve the spectral rendering. However, for many operational scenarios for airborne remote-sensing image data input to a data-driven fire propagation model, the use of a complicated rendering model like DIRSIG may not be necessary. Future work will examine the potential to simplify the procedures described here. For example, fire propagation codes that consider simpler flame shapes than our voxelized structure within their radiation transfer calculations could be used to estimate the direct and reflected radiation. Further, precomputed atmospheric transmission properties in a 'look-up' table could be used to estimate atmospheric effects on the radiation reaching the sensor. These changes would allow a tighter coupling between the dynamic fire propagation model and the remote-sensing image data and reduce computational requirements.

Acknowledgements

The present material is based on work supported by the National Science Foundation under grant numbers CNS-0324989 and CNS-0324910 and by the National Aeronautics and Space Administration under grant number NAG5–10051.

References

Ambrosia V, Wegener S, Sullivan D, Buechel S, Dunagan S, Brass J, Stoneburner J, Schoenung S (2003) Demonstrating UAV-acquired real-time thermal data over fires. *Photogrammetric Engineering and Remote Sensing* **69**, 391–402.

Anderson GP, Berk A, Acharya PK, Matthew MW, Bernstein LS, Chetwynd JH, Dothe H, Adler-Golden SM, Ratkowski AJ, Felde GW, Gardner JA, Hoke ML, Richtsmeier SC, Pukall B, Mello J, Jeong LS (2000) MODTRAN4: Radiative transfer modeling for remote sensing. In 'Algorithms for Multispectral, Hyperspectral, and Ultraspectral Imagery VI'. (Eds SS Chen, MR Descour) Proceedings of SPIE, Vol. 4049, pp. 176–183. (SPIE: Bellingham, WA)

Anderson JL (1996) A method of producing and evaluating probabilistic forecasts from ensemble model integrations. *Journal of Climate* **9**, 1518–1530. doi:10.1175/1520-0442(1996)009<1518:AMFPAE>2.0.CO;2

Asensio MI, Ferragut L (2002) On a wildland fire model with radiation. *International Journal for Numerical Methods in Engineering* **54**, 137–157. doi:10.1002/NME.420

Barker DM, Huang W, Guo YR, Xiao QN (2004) A three-dimensional (3DVAR) data assimilation system for use with MM5: implementation and initial results. *Monthly Weather Review* **132**, 897–914. doi:10.1175/1520-0493(2004)132<0897:ATVDAS>2.0.CO;2

Brown AA, Davis KP (1973) 'Forest fire control and use.' 2nd edn. (McGraw-Hill: New York)

Clark TL, Jenkins MA, Coen J, Packham D (1996) A coupled atmosphere–fire model: convective feedback on fire-line dynamics. *Journal of Applied Meteorology* **35**, 875–901. doi:10.1175/1520-0450(1996)035<0875:ACAMCF>2.0.CO;2

Clark TL, Coen JL, Latham D (2004) Description of a coupled atmosphere–fire model. *International Journal of Wildland Fire* **13**, 49–63. doi:10.1071/WF03043

Coen JL (2005) Simulation of the Big Elk Fire using coupled atmosphere–fire modeling. *International Journal of Wildland Fire* **14**, 49–59. doi:10.1071/WF04047

Darema F (2004) Dynamic data-driven applications systems: a new paradigm for application simulations and measurements. *Lecture Notes in Computer Science* **3038**, 662–669. doi:10.1007/B97989

Dennison PE (2006) Fire detection in imaging spectrometer data using atmospheric carbon dioxide absorption. *International Journal of Remote Sensing* **27**, 3049–3055. doi:10.1080/01431160600660871

Derber J, Rosati A (1989) A global oceanic data assimilation system. *Journal of Physical Oceanography* **19**, 1333–1347. doi:10.1175/1520-0485(1989)019<1333:AGODAS>2.0.CO;2

Digital Imaging and Remote Sensing Laboratory (2006) 'The DIRSIG User's Manual.' (Rochester Institute of Technology: Rochester, NY) Available at http://www.dirsig.org/docs/manual-2006-11.pdf [Verified 30 April 2009]

Douglas CC, Beezley JD, Coen J, Li D, Li W, Mandel AK, Mandel J, Qin G, Vodacek A (2006) Demonstrating the validity of a wildfire DDDAS. *Lecture Notes in Computer Science* **3993**, 522–529. doi:10.1007/11758532_69

Drysdale D (1998) 'An Introduction to Fire Dynamics.' 2nd edn. (Wiley: Chichester, UK)

Finney MA (1998) FARSITE: Fire Area Simulator-Model, development and evaluation. USDA Forest Service, Rocky Mountain Research Station Paper, RMRS-RP-4. (Ogden, UT)

Greenfield PH, Smith W, Chamberlain DC (2003) Phoenix – the new Forest Service airborne infrared fire detection and mapping system. In '5th Symposium on Fire and Forest Meteorology and the 2nd International Wildland Fire Ecology and Fire Management Congress', 16–20 November 2003, Orlando, FL. Paper J1G.3. (American Meteorological Society: Boston, MA)

Kaufman Y, Remer L, Ottmar R, Ward D, Li R-R, Kleidman R, Fraser R, Flynn L, McDougal D, Shelton G (1996) Relationship between remotely sensed fire intensity and rate of emission of smoke: SCAR-C experiment. In 'Global Biomass Burning'. (Ed. J Levine) pp. 685–696. (MIT Press: Cambridge, MA)

Knight IK, Sullivan AL (2004) A semi-transparent model of bushfire flames to predict radiant heat flux. *International Journal of Wildland Fire* **13**, 201–207. doi:10.1071/WF03047

Kremens R, Faulring J, Hardy C (2003) Measurement of the time–temperature and emissivity history of the burn scar for remote sensing applications. In '5th Symposium on Fire and Forest Meteorology and the 2nd International Wildland Fire Ecology and Fire Management Congress', 16–20 November 2003, Orlando, FL. Paper J1G.5. (American Meteorological Society: Boston, MA)

Lentile LB, Holden ZA, Smith AMS, Falkowski MJ, Hudak AT, Morgan P, Lewis SA, Gessler PE, Benson NC (2006) Remote sensing techniques to assess active fire characteristics and post-fire effects. *International Journal of Wildland Fire* **15**, 319–345. doi:10.1071/WF05097

Linn RR (1997) Transport model for prediction of wildfire behavior. Los Alamos National Laboratory, Scientific Report LA13334-T. (Los Alamos, NM)

Malanotte-Rizzoli P, Tziperman E (1996) The oceanographic data assimilation problem: overview, motivation and purposes. In 'Modern Approaches to Data Assimilation in Ocean Modeling'. (Ed. P Malanotte-Rizzoli) pp. 3–17. (Elsevier: Amsterdam)

Mandel J, Bennethum LS, Beezley JD, Coen JL, Douglas CC, Kim M, Vodacek A (2008) A wildland fire model with data assimilation. *Mathematics and Computers in Simulation* **79**, 584–606. doi:10.1016/J.MATCOM.2008.03.015

McGrattan K, Klein B, Hostikka S, Floyd J (2007) Fire Dynamics Simulator (Version 5) User's Guide. NIST Building and Fire Research Laboratory. NIST Special Publication 1019-5. (Washington, DC)

McKeown D, Cockburn J, Faulring J, Kremens R, Morse D, Rhody H, Richardson M (2005) Wildfire Airborne Sensor Program (WASP): a new wildland fire detection and mapping system. In 'Proceedings of the Tenth Forest Service Remote Sensing Applications Conference', 5–9 April 2004, Salt Lake City, UT. (Ed. JD Greer) (CD-ROM) (American Society for Photogrammetry and Remote Sensing: Bethesda, MD)

Mell W, Jenkins MA, Gould J, Cheney P (2007) A physics-based approach to modeling grassland fires. *International Journal of Wildland Fire* **16**, 1–22. doi:10.1071/WF06002

Pastor E, Zárate L, Planas E, Arnaldos J (2003) Mathematical models and calculation systems for the study of wildland fire behaviour. *Progress in Energy and Combustion Science* **29**, 139–153. doi:10.1016/S0360-1285(03)00017-0

Press WH, Teukolsky SA, Vetterling WT, Floannery BP (2007) 'Numerical Recipes 3rd edn: the Art of Scientific Computing.' (Cambridge University Press: Cambridge, MA)

Radke L, Clark TL, Coen JL, Walther CA, Lockwood R, Riggan PJ, Brass J, Higgins RW (2000) The WildFire experiment: observations with airborne remote sensors. *Canadian Journal of Remote Sensing* **26**, 406–417.

Riggan PJ, Tissel RG, Lockwood RN, Brass JA, Pereira JAR, Miranda HS, Miranda AC, Campos T, Higgins R (2004) Remote measurement of energy and carbon flux from wildfires in Brazil. *Ecological Applications* **14**, 855–872. doi:10.1890/02-5162

Rothermel RC (1972) A mathematical model for predicting fire spread in wildland fuels. USDA Forest Service, Forest Service Intermountain Forest and Range Experiment Station, Research Paper INT-115. (Ogden, UT)

Schott JR, Brown SD, Raqueño RV, Gross HN, Robinson G (1999) An advanced synthetic image generation model and its application to multi/hyperspectral algorithm development. *Canadian Journal of Remote Sensing* **25**, 99–111.

Vodacek A, Kremens RL, Fordham AJ, VanGorden SC, Luisi D, Schott JR, Latham DJ (2002) Remote optical detection of biomass burning using a potassium emission signature. *International Journal of Remote Sensing* **23**, 2721–2726. doi:10.1080/01431160110109633

Weber RO (1991) Toward a comprehensive wildfire spread model. *International Journal of Wildland Fire* **1**, 245–248. doi:10.1071/WF9910245

Wooster MJ, Zhukov B, Oertel D (2003) Fire radiative energy for quantitative study of biomass burning: derivation from the BIRD experimental satellite and comparison to MODIS fire products. *Remote Sensing of Environment* **86**, 83–107. doi:10.1016/S0034-4257(03)00070-1

Manuscript received 29 May 2007, accepted 16 May 2008